fractal and fractional

MDPI

Article

Morphology-Controlled Single Rock Particle Breakage: A Finite-Discrete Element Method Study with Fractal Dimension Analysis

Ruidong Li [1], Shaoheng He [1,*], Haoran Jiang [2], Chengkai Xu [1] and Ningyu Yang [3]

[1] Department of Civil and Environmental Engineering, The Hong Kong Polytechnic University, Hong Kong SAR, China; 21054468g@connect.polyu.hk (R.L.); 22064176g@connect.polyu.hk (C.X.)
[2] Civil Engineering Design Division, Kajima Corporation, Tokyo 107-8477, Japan; jiangh@kajima.com
[3] School of Transportation Science and Engineering, Harbin Institute of Technology, Harbin 150090, China; nyyang97@gmail.com
* Correspondence: shaoheng.he@polyu.edu.hk

Abstract

This study investigates the influence of particle morphology on two-dimensional (2D) single rock particle breakage using the combined finite-discrete element method (FDEM) coupled with fractal dimension analysis. Three key shape descriptors (elongation index *EI*, roundness index *Rd*, and roughness index *Rg*) were systematically varied to generate realistic particle geometries using the Fourier transform and inverse Monte Carlo. Numerical uniaxial compression tests revealed distinct morphological influences: *EI* showed negligible impact on crushing strength or fragmentation, and *Rd* significantly increased crushing strength and fragmentation due to improved energy absorption and stress distribution. While *Rg* reduced strength through stress concentration at asperities, suppressing fragmentation and elastic energy storage. Fractal dimension analysis demonstrated an inverse linear correlation with crushing strength, confirming its predictive value for mechanical performance. The validated FDEM framework provides critical insights for optimizing granular materials in engineering applications requiring morphology-controlled fracture behavior.

Keywords: FDEM; particle breakage; particle shape; fractal dimension

Academic Editor: Alex Elías-Zúñiga

Received: 31 July 2025
Revised: 18 August 2025
Accepted: 20 August 2025
Published: 26 August 2025

Citation: Li, R.; He, S.; Jiang, H.; Xu, C.; Yang, N. Morphology-Controlled Single Rock Particle Breakage: A Finite-Discrete Element Method Study with Fractal Dimension Analysis. *Fractal Fract.* **2025**, *9*, 562. https://doi.org/10.3390/fractalfract9090562

1. Introduction

Particle breakage fundamentally governs the mechanical behavior of granular assemblies across critical engineering domains, including geotechnical infrastructure, mineral processing, and natural resource exploitation [1–4]. The breakage characteristics of individual particles directly influence macroscale responses such as shear strength evolution, compaction behavior, and permeability reduction in granular media [5–7]. Traditional experimental approaches, exemplified by single-particle compression tests and drop-weight impact studies, have established empirical correlations between crushing strength, particle size, and mineral composition [8,9]. However, these methods face inherent limitations in isolating the explicit contribution of morphological complexity, such as the interplay of particle elongation, angularity, and surface texture, to fracture initiation and propagation dynamics under quasi-static loading [10,11].

Computational modelling offers a viable pathway to address mechanical problems, such as the finite element method (FEM) [12,13], material point method (MPM) [14–17], and particle-finite element method (PFEM) [18]. Compared to these numerical methods,

the discrete element method (DEM) and bonded particle model (BPM) frameworks offer deeper insights into granular fracture mechanics. However, their reliance on spherical or polyhedral particle idealizations introduces significant simplifications [19,20]. Such geometric approximations fail to capture stress concentrations arising from natural surface irregularities and angular features, resulting in systematic underestimation of fracture energy dissipation and inaccuracies in fragment size distribution predictions [21,22]. Prior studies to enhance shape fidelity in DEM, such as clumped spheres, convex polyhedra and level-set particles, still model fracture via contact or cohesive bond breakage between rigid particles and do not resolve crack initiation and propagation within grains [23–25].

The combined finite-discrete element method (FDEM) resolves this limitation by coupling continuum finite elements with discrete fracture networks [26]. Through the embedding of cohesive elements within a deformable solid matrix, FDEM enables explicit simulation of tensile and shear crack propagation governed by traction-separation constitutive laws. This technique integrates the benefits of both the FEM and DEM into a whole framework [27]. The FEM is responsible for calculating the elastic deformation of the solid continuum, while the DEM determines the interaction and fracture of discrete bodies [28,29]. Compared with the conventional FEM, zero-thickness cohesive elements that follow specific fracture criteria are embedded between solid elements to mimic the crack propagation in FDEM. Despite its theoretical rigor, broader implementation of FDEM for morphology-dependent studies remains constrained by two factors: (i) inadequate computational protocols for generating high-fidelity particle libraries with controlled morphological variance, and (ii) insufficient quantification of correlations between multidimensional shape descriptors and fracture metrics.

Furthermore, fractal geometry has become a ubiquitous analytical tool across diverse disciplines such as medicine, materials science, and geography. While prior work has established that the breakage patterns of granular materials exhibit fractal characteristics quantifiable by a fractal dimension [30], investigations into the geometric attributes of particles via fractal analysis have primarily been confined to two dimensions, as exemplified by the study of Arasan et al. [31]. However, its adoption within geotechnical engineering, particularly concerning single-particle fragmentation, remains comparatively limited.

This study establishes an integrated computational framework combining Fourier-based shape reconstruction, fractal dimension analysis, and two-dimensional (2D) FDEM simulation. Leveraging Fourier descriptor theory, particle morphology is parameterized through harmonic coefficients that map directly to standardized shape indices—elongation index, roundness index, and roughness index. An inverse Monte Carlo sampling algorithm enforces statistical consistency between synthesized particles and target morphological distributions. This integration enables systematic interrogation of how particle morphologies and fractal dimensions govern crushing strength and fragment-size distributions. The influence of particle morphologies and fractal dimensions on particle crushing strength is systematically investigated.

2. Methods

2.1. Principle of FDEM

In 2D FDEM, the solid continuum is discretized into triangular finite elements interconnected by zero-thickness cohesive elements [32]. The kinematic behavior of each element is governed by nodal forces, which are resolved through an explicit second-order central difference time integration scheme at each computational step. These nodal forces comprise three components: internal resisting forces, externally applied loads, and damping forces. Following force computation, nodal accelerations are determined at the beginning

of the time increment, enabling subsequent updates to nodal velocities and displacements. Typically, the governing equation of the FDEM system is expressed as:

$$\boldsymbol{M}\frac{\partial^2 \boldsymbol{x}}{\partial t^2} + \boldsymbol{C}\frac{\partial \boldsymbol{x}}{\partial t} + \boldsymbol{F}_{\text{int}}(\boldsymbol{x}) - \boldsymbol{F}_{\text{ext}}(\boldsymbol{x}) - \boldsymbol{F}_c(\boldsymbol{x}) = 0 \tag{1}$$

where $\boldsymbol{M}$ is the lumped mass matrix of the system; $\boldsymbol{C}$ denotes the diagonal damping matrix of the system; $\boldsymbol{x}$ represents the nodal displacement; $\boldsymbol{F}_{\text{int}}$, $\boldsymbol{F}_{\text{ext}}$, and $\boldsymbol{F}_c$ denote the internal resisting forces, the applied external loads, and the contact forces, respectively.

To simulate the fracture progression in FDEM, the cohesive elements adhere to a prescribed linear traction-separation (T-S) model, as shown in Figure 1. The linear T-S model typically comprises two distinct stages: the linear elastic stage and the linear damage stage. In the linear elastic stage, the material properties of cohesive elements remain constant and is defined as follows:

$$\boldsymbol{t} = \begin{Bmatrix} t_n \\ t_s \end{Bmatrix} = \begin{bmatrix} E_{nn} & E_{ns} \\ E_{ns} & E_{ss} \end{bmatrix} \begin{Bmatrix} \varepsilon_n \\ \varepsilon_s \end{Bmatrix} = \boldsymbol{E}\boldsymbol{\varepsilon} = \frac{1}{T_0}\boldsymbol{K}\boldsymbol{\delta} \tag{2}$$

where $\boldsymbol{t}$ denotes the nominal traction stress; $\boldsymbol{\varepsilon}$ represents the nominal strain; $\boldsymbol{E}$ denotes the elastic modulus; T_0 is the initial thickness of the cohesive elements; $\boldsymbol{\delta}$ represents the displacement of the cohesive elements; and $\boldsymbol{K}$ is the stiffness matrix. Notably, the subscript n denotes 'normal direction' and s represents 'shear direction'. For example, t_n and t_s represent the traction in the normal (mode I) and shear (mode II) direction, respectively [27,32]. The constitutive thickness of cohesive elements is typically set to 1, while the geometric thickness defaults to 0, ensuring that the nodal separation displacement equals the nominal strain. To determine the initiation of damage evolution or the linear damage stage, the quadratic nominal stress criterion (QUADS) is used:

$$\left\{\frac{\langle t_n \rangle}{t_{n0}}\right\}^2 + \left\{\frac{t_s}{t_{s0}}\right\}^2 = 1 \tag{3}$$

where $\langle\rangle$ denotes the Macaulay bracket; t_{n0} and t_{s0} represent pure traction at damage initiation in the normal and shear directions, respectively. Once damage initiates, the T-S model follows a linear softening law (see Figure 1). A damage variable D is introduced to quantify the progression of damage, evolving from 0 (undamaged) to 1 (fully damaged). When $D = 1$, the cohesive element reaches its ultimate load-bearing capacity, leading to its removal and the formation of free surfaces, thereby marking the onset of crack propagation. The damage variable D is computed as:

$$D = \sqrt{D_n^2 + D_s^2} \tag{4}$$

$$D_n = \frac{\delta_n^f\left(\delta_n^{max} - \delta_n^0\right)}{\delta_n^{max}\left(\delta_n^f - \delta_n^0\right)}, \delta_n^{max} \geqslant 0 \tag{5}$$

$$D_s = \frac{\delta_s^f\left(\delta_s^{max} - \delta_s^0\right)}{\delta_s^{max}\left(\delta_s^f - \delta_s^0\right)} \tag{6}$$

where D_n and D_s denote the damage variables in the normal and shear direction, respectively; δ_n^0 and δ_n^{max} represent the effective separation at damage initiation and the maximum effective separation attained during the loading history in the normal direction; δ_s^0 and δ_s^{max} are the effective separation at damage initiation and the maximum effective separation attained during the loading history in the shear direction; δ_n^f and δ_s^f denote the effective

separation at complete failure in normal and shear direction, respectively, and expressed as follows:

$$\delta_n^f = 2G_I^C / t_n^0 \tag{7}$$

$$\delta_s^f = 2G_{\mathrm{II}}^C / t_s^0 \tag{8}$$

where G_I^C, and G_{II}^C represent the critical fracture energy in the normal and shear direction, respectively. Once the D is obtained, the degradation of the normal and shear stiffness as well as normal and shear traction of the cohesive elements is also determined until final failure as follows:

$$t_n = \begin{cases} (1-D)k_n\delta_n, & \delta_n \geq 0 \text{ (tension)} \\ k_n\delta_n, & \delta_n < 0 \text{ (compression)} \end{cases} \tag{9}$$

$$t_s = (1-D)k_s\delta_s \tag{10}$$

The final failure of cohesive elements is usually described from the view of displacement or fracture energy. This implies that when the displacement or fracture energy dissipated by the cohesive element exceeds a certain threshold, the cohesive element is broken and deleted. The power-law criterion is the most extensively utilized fracture energy criterion for predicting damage progression under mixed-mode loads, which is described as follows:

$$\left(\frac{G_I}{G_{IC}}\right)^2 + \left(\frac{G_{II}}{G_{IIC}}\right)^2 = 1 \tag{11}$$

where G_{IC} and G_{IIC} denote fracture energies in pure mode I and mode II, respectively. G_I and G_{II} represent energies dissipated in pure mode I and mode II, respectively. Once the above criterion is met, the cohesive element will be deleted to describe local failure in the simulation.

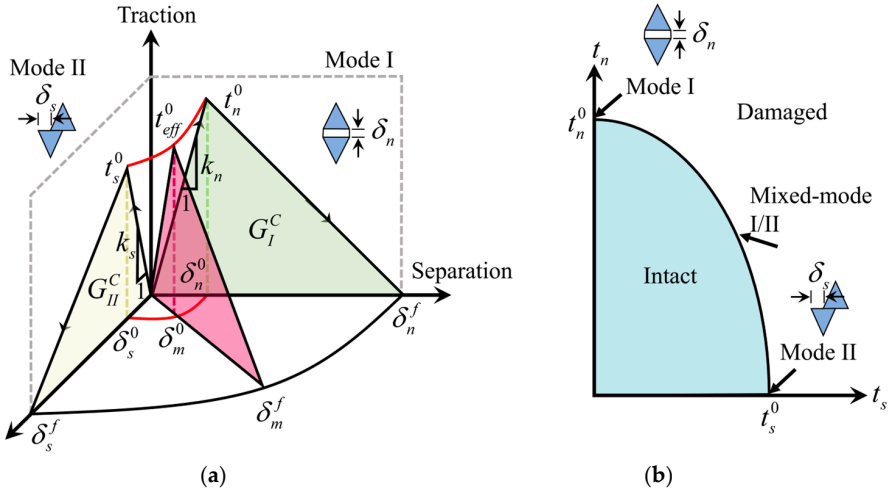

Figure 1. Constitutive model of cohesive elements: (**a**) mixed-mode linear traction-separation behavior and (**b**) mixed-mode damage initiation criterion.

2.2. Shape Indexes and Fractal Dimensions

Particle morphology is generally evaluated by shape indexes. In this study, three common shape indexes are used: elongation index (EI), roundness index (Rd), and roughness index (Rg), defined as follows [33,34]:

$$EI = \frac{L_{\mathrm{minor}}}{L_{\mathrm{major}}} \tag{12}$$

$$Rd = \sum_{i=1}^{N_C} R_i / (N_C \cdot R_{\max}) \tag{13}$$

$$Rg = \frac{\sqrt{\frac{\sum(r_\theta - r'_\theta)^2}{N_R}}}{\overline{r_\theta}} \tag{14}$$

where L_{minor} and L_{major} represent the minor and major dimensions of the particle; N_C denotes the number of corners; R_i is the radius of curvature of the ith corner; $R_{\max}$ represents the radius of the maximum inscribed circle; N_R denotes the total number of the discretized points of the particle contour; r_θ is the radial distance of the discretized point at a polar angle θ along the original contour of the particle; $\overline{r_\theta}$ denotes the average value of r_θ; and r'_θ represents the radial distance of the discretized point at a polar angle θ along the smoothed particle outline. Note that all curvatures in this study are calculated based on the discrete corner approximation [35].

To quantify the 2D fractal dimension F_D of the particle, a voxelized 2D projection of the particle is first generated. Then, the box-counting method [36] is adopted as follows:

$$F_D = \lim_{r \to 0} \frac{\log(N_r)}{\log(1/r)} \tag{15}$$

where r denotes the cube size, varying from the smallest unit in the voxel scale to half of the total volume dimension, and N_r represents the number of cubes containing the particle in the r scale. The minimum box size is set to one voxel, and the maximum box size is set to half the maximum dimension of the particle, respectively. More details about the computation of 2D fractal dimensions of particles can be found in [37].

2.3. Fourier Description of Particle Shape

Consider a 2D star-like particle with the center point at $O(x_0, y_0)$, the particle contour can be represented by N_p points P_i at a specified angle θ_p around O in the Cartesian coordinate system. The coordinates of each point P_i (x_i, y_i) in the Cartesian coordinate system can be described by an angle θ_i and distance r_i in the polar coordinate system, expressed as follows:

$$\begin{cases} x_i = x_0 + r_i cos\theta_i \\ y_i = y_0 + r_i sin\theta_i \end{cases} \tag{16}$$

Based on the discrete Fourier transform (DFT), the relationship between θ_i and r_i can be modified as follows:

$$\frac{r_i(\theta_i)}{r_0} = AF \times \{1 + \sum_{n=1}^{N} [D_n sin(n\theta_i + \varphi_n)]\} \tag{17}$$

where AF represents the amplification factor that determines the size of the particle; N denotes the total number of harmonics; r_0 denotes the average radius of the particle; Then, the Fourier descriptors F_n is calculated as follows:

$$F_n = \frac{\sqrt{A_n^2 + B_n^2}}{r_0} \tag{18}$$

where A_n and B_n are the amplitude of the sinusoidal signal f_n in the frequency domain. Therefore, the first Fourier descriptor F_0 is equal to 1 due to the normalization, since $\sqrt{A_n^2 + B_n^2} = r_0$. F_1 represents a positional shift of the shape contour relative to point O, typically set to 0 due to its ignorable influence on particle shapes. In contrast, F_2 is a crucial parameter as it quantifies EI. Previous studies have demonstrated that descriptors F_3 to F_{16} primarily define contour roundness, while higher-order modes (F_n for $n > 16$) effectively characterize surface roughness. Accordingly, Fourier descriptors can be categorized into five distinct groups: F_0, F_1, F_2, $F_3 - F_{16}$ and $F_{16} - F_n$, where $F_3 - F_{16}$ and $F_{16} - F_n$ satisfies the following equations:

$$F_n = 2^{-2 \cdot log_2(\frac{n}{3}) + log_2(F_3)},\ 3 < n < 16 \tag{19}$$

$$F_n = 2^{-2 \cdot log_2(\frac{n}{8}) + log_2(F_{16})},\ 16 \leq n < N \tag{20}$$

In this study, a value of $N = 64$ was selected to ensure computational efficiency. Following the methodology established by [38], the parameters were set as $F_0 = 1$, $\varphi_0 = \pi/2$, and $F_1 = 0$ to normalize the average particle radius $r_0 = 1$ and center the particle at the coordinate origin O before amplification. Under these conditions, Formula (17) simplifies to:

$$r(\theta) = \mathrm{AF} \times \left\{ f_0 + f_1 + \sum_{n=2}^{N} [F_n \cdot sin(n\theta + \varphi_n)] \right\} \tag{21}$$

where $f_0 = F_0 \cdot sin(0 \times \theta + \varphi_0) = 1$ and $f_1 = F_1 \cdot sin(1 \times \theta + \varphi_1) = 0$. Importantly, Previous studies have demonstrated strong correlations between key Fourier descriptors (F_2, F_3 and F_{16}) and conventional particle shape indicators (EI, Rd, and Rg) [38,39]. For example, [40] created a comprehensive database of over 1.5 million particles and performed regression analysis to establish empirical relationships between key shape descriptors (EI, Rd, and Rg) and Fourier descriptors (F_2, F_3 and F_{16}). The resulting statistical correlations are expressed as:

$$F_2 = -0.48\left(EI^t\right)^2 + 0.17\left(EI^t\right) + 0.33 \tag{22}$$

$$F_3 = 0.14\left(Rd^t\right)^2 - 0.40\left(Rd^t\right) + 0.26 \tag{23}$$

$$F_{16} == 90.8634\left(Rg^t\right) + 0.0002 \tag{24}$$

where EI^t, Rd^t, and Rg^t represent the target EI, Rd and Rg, respectively. These validated equations provide a robust quantitative link between geometric descriptors and Fourier coefficients and will serve as the foundation for particle generation in this study. By implementing these relationships within an efficient algorithmic framework, particles can be systematically produced to match specified shape characteristics (see Figure 2), enabling the creation of diverse particle populations with controlled morphological properties.

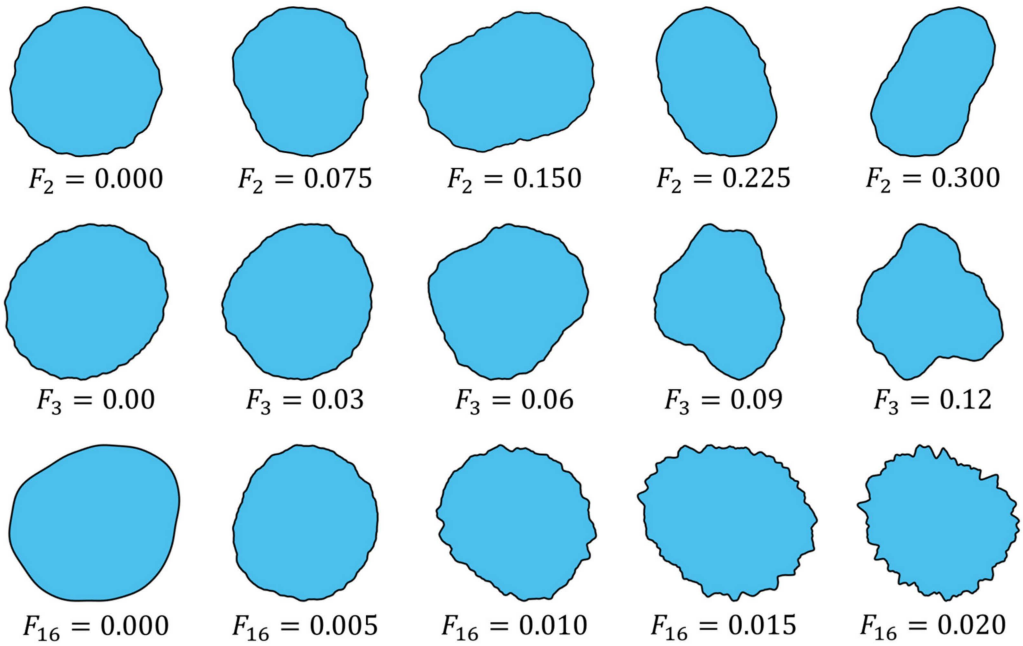

Figure 2. Reconstruction of 2D particle contours based on different Fourier descriptors.

2.4. Particle Shape Acquisition

Although X-ray tomography provides a method for acquiring realistic particle shapes, it is cost-prohibitive and challenging to acquire abundant shapes [41,42]. Therefore, the inverse Monte Carlo approach [43] is employed to generate abundant particle shapes with desirable characteristics. This method employs a relative error metric e_r to quantify the similarity between reconstructed and target particle shapes, defined as:

$$e_{ri}^{SD} = \frac{|SD_i - SD_i^t|}{SD_i} \times 100\% \tag{25}$$

where SD_i represents the computed shape descriptors (EI, Rd and Rg) of the generated ith particle; and SD_i^t is denotes the corresponding target descriptor values. The particle generation algorithm proceeds through the following steps (see Figure 3):

(a) Assign the target shape indicators (EI^t, Rd^t and Rg^t) and the threshold of relative error e_{th}.

(b) Substitute the target values into formulas (22)–(24) to obtain the Fourier amplitude coefficients (F_2, F_3 and F_{16}) for particle reconstruction.

(c) Use the inverse discrete Fourier transform (IDFT) and random phase angles in Section 2.3 to reconstruct the particles based on the obtained Fourier amplitude coefficients (F_2, F_3 and F_{16}) in step (b). Other Fourier amplitude coefficients are determined by formulas (19) and (20). The phase angle ranges from $-\pi$ to π.

(d) Evaluate the reconstructed particles by shape indexes and obtain the value of reconstructed shape indicators (EI_i, Rd_i and Rg_i). Based on Formula (25), calculate the relative error (e_{ri}^{EI}, e_{ri}^{Rd} and e_{ri}^{Rg}) between reconstructed shape indicators (EI_i, Rd_i and Rg_i) with the target shape indicators (EI^t, Rd^t and Rg^t). If the calculated relative error (e_{ri}^{EI}, e_{ri}^{Rd} and e_{ri}^{Rg}) is larger than the threshold of relative error e_{th}, the generated particle will be deleted and back to step (b).

(e) Repeat step (c) until the target number of particles is reconstructed successfully.

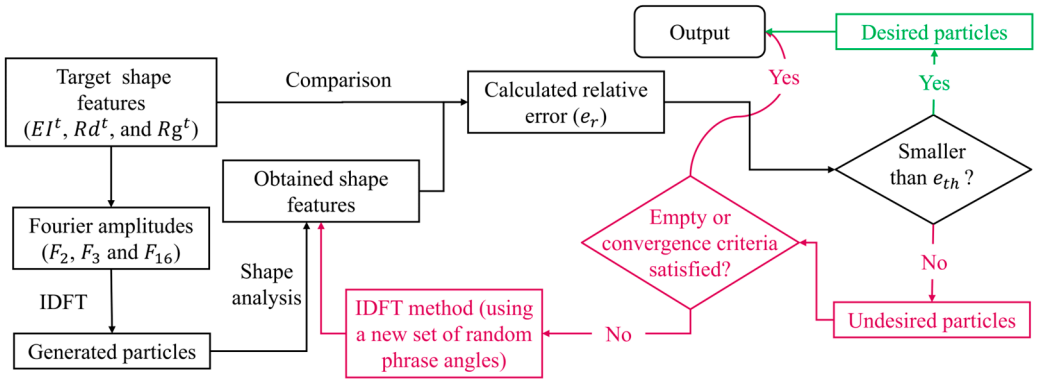

Figure 3. Flowchart of the acquisition of desired particles.

2.5. Particle Crushing Strength

For a single particle, the particle crushing strength σ_f is quantified by the formula proposed by Hiramatsu and Oka (1966):

$$\sigma_f = \frac{0.9F}{d^2} \tag{26}$$

where F denotes the first major peak of the force–displacement curve; and d is the equivalent diameter of the particle, which refers to the circle-equivalent diameter based on

cross-section. Based on the Weibull distribution function [44,45], the cumulative survival probability function for a given single particle is expressed as follows:

$$P_s(\sigma_f) = exp\left[-\left(\frac{\sigma_f}{\sigma_0}\right)^m\right] \tag{27}$$

where σ_f is the particle crushing strength; and m denotes the Weibull modulus that represents the variability in the crushing strength of different particles; and σ_0 denotes the particle crushing strength with a survival probability of 36.8%. Both the two parameters, i.e., m and σ_0, are estimated by experimentally rewriting Formula (27) as:

$$ln\left[ln\left(1/P_s\left(\sigma_f\right)\right)\right] = mln\sigma_f - mln\sigma_0 \tag{28}$$

In this study, for a finite number of examined particles, first, the data is sorted in ascending order of particle crushing strength σ_{fi}, and then cumulative survival probability P_{si} can be determined by the rank position:

$$P_{si} = 1 - \frac{i}{N+1} \tag{29}$$

where i represents the rank of the particle sorted in ascending order, and N denotes the total number of particles tested. By fitting the data with the best straight line, the relationship between $ln[ln(1/P_s\left(\sigma_f\right))]$ and $ln\sigma_f$ can be obtained. The Weibull modulus m and value of σ_0 can be obtained from the slope and the intercept of Formula (28). The Weibull modulus, m, gives information on the spread of the distribution of strength and, therefore, on the number of defects present in the sample. The higher the value of m, the more homogeneous the sample.

3. Numerical Simulation

3.1. Model Calibration

To validate the efficacy of the FDEM in simulating single-particle rock fragmentation, a numerical uniaxial compression test was conducted using the commercial finite element analysis software ABAQUS 2021 [46]. Figure 4 illustrates the numerical model configuration, which comprises a rock specimen positioned between two steel loading platens in perfect contact (zero-gap condition). While maintaining consistency between numerical and experimental loading rates would be theoretically ideal, computational constraints necessitated a compromise between solution accuracy and computational efficiency. The boundary conditions for the elements in the bottom loading plate are fixed, while other elements are unfixed. Therefore, a modified loading rate of 0.1 mm/s, previously validated by [47], was implemented. In the simulation, the upper loading platen was displaced at this constant velocity while the lower platen remained fully constrained. The rock particle specimen had a nominal diameter of 50 mm.

To account for the stochastic nature of fracture propagation, a comprehensive network of four-node cohesive elements was systematically embedded between all adjacent triangular solid element vertices during model preparation. This was achieved through an automated process utilizing a custom-developed Python (v3.12) script to ensure computational efficiency. The discretized model consisted of three-node plane strain triangular elements (CPE3) and two-dimensional four-node cohesive elements (COH2D4), as shown in Figure 5. Figure 6 presents the mesh size sensitivity analysis through load–displacement curves and von Mises stress distributions. The results indicate that a larger mesh size leads to an earlier and higher peak load compared to experimental data. This premature elevation may arise because a smaller mesh size increases the local contact area with the platens,

thereby raising the failure stress. To balance computational efficiency with accuracy, a mesh size of 1 mm was adopted for all simulations in this study.

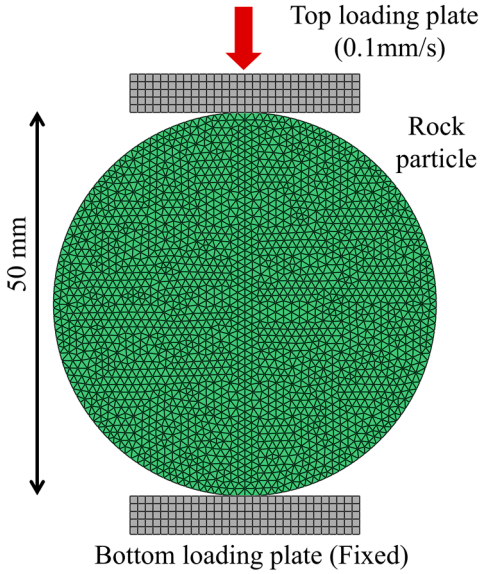

Figure 4. Schematic diagram of the single particle uniaxial compression test.

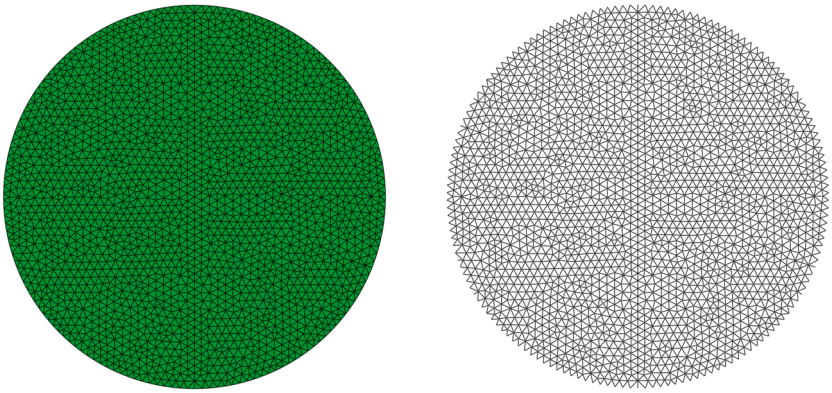

(**a**) (**b**)

Figure 5. Illustrations of: (**a**) solid elements; and (**b**) cohesive elements.

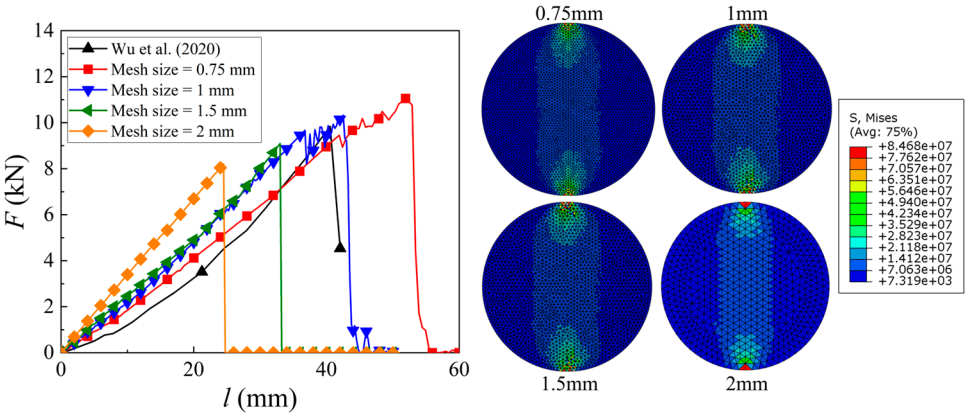

(**a**) (**b**)

Figure 6. Sensitivity analysis on: (**a**) mesh sizes through force–displacement curves [48]; and (**b**) von Mises stress distributions.

Accurate mechanical parameter calibration is essential for reliable FDEM simulations, as fracture behavior is highly sensitive to material properties. This study calibrated parameters using experimental data from [47] on sandstone particle crushing. The calibrated load–displacement curve, obtained through systematic parameter optimization, shows excellent agreement with experimental data (Figure 6). More specifically, the dominant crack propagates parallel to the loading direction. The experimental results yield a peak compressive strength of 9.5 MPa at an axial strain of 0.43%, while the numerical simulation demonstrates a closely matched peak strength of 10.0 MPa at a corresponding axial strain of 0.44%. This close agreement in both peak strength and critical strain underscores the validity of the simulation. Furthermore, the failure modes in the experiment and simulation are virtually identical (Figure 7). In both cases, a primary crack penetrates the particle, accompanied by secondary fractures initiating at the contact interfaces between the particle and the loading platens. These observations confirm the appropriateness of the calibrated parameters. The finalized material parameters adopted in the numerical simulations are summarized in Table 1.

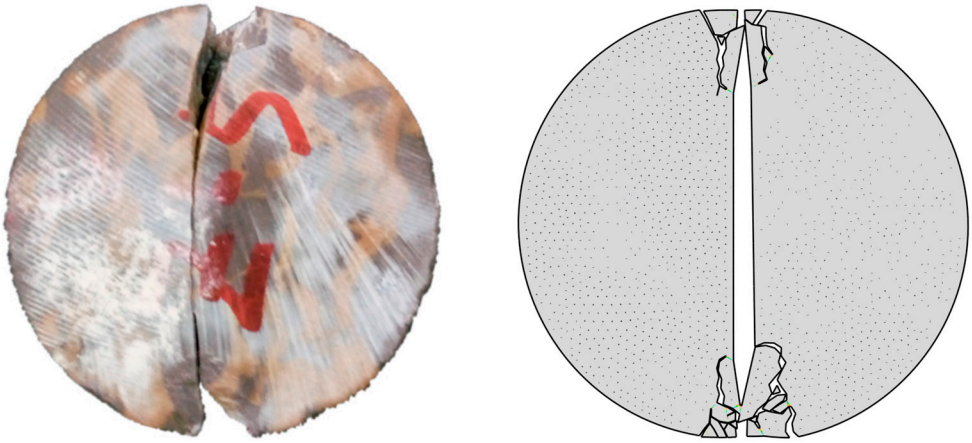

(**a**) (**b**)

Figure 7. Comparison of crushing patterns: (**a**) crushing pattern in the experiment and (**b**) crushing pattern in the calibration result.

Table 1. Micro-parameters used in DEM simulation.

Materials	Parameters	Values
Loading plates	Density	7.8×10^3
	Young's modulus (GPa)	2.1×10^2
	Poisson's ratio	0.3
Solid elements	Density	2.5×10^3
	Young's modulus (GPa)	15
	Poisson's ratio	0.3
Cohesive elements	Initial tensile stiffness (GPa·m^{-1})	9.5
	Initial shear stiffness (GPa·m^{-1})	17.6
	Normal traction force (MPa)	5
	Tangential traction force (MPa)	18
	Model-I fracture energy (N·mm^{-1})	60
	Model-II fracture energy (N·mm^{-1})	165

3.2. Model Setup

To account for irregular particle shapes in FDEM simulations, the aforementioned shape descriptors (EI, Rd, and Rg) were employed with varying target values to generate representative rock particles (Figure 8), as summarized in Table 2.

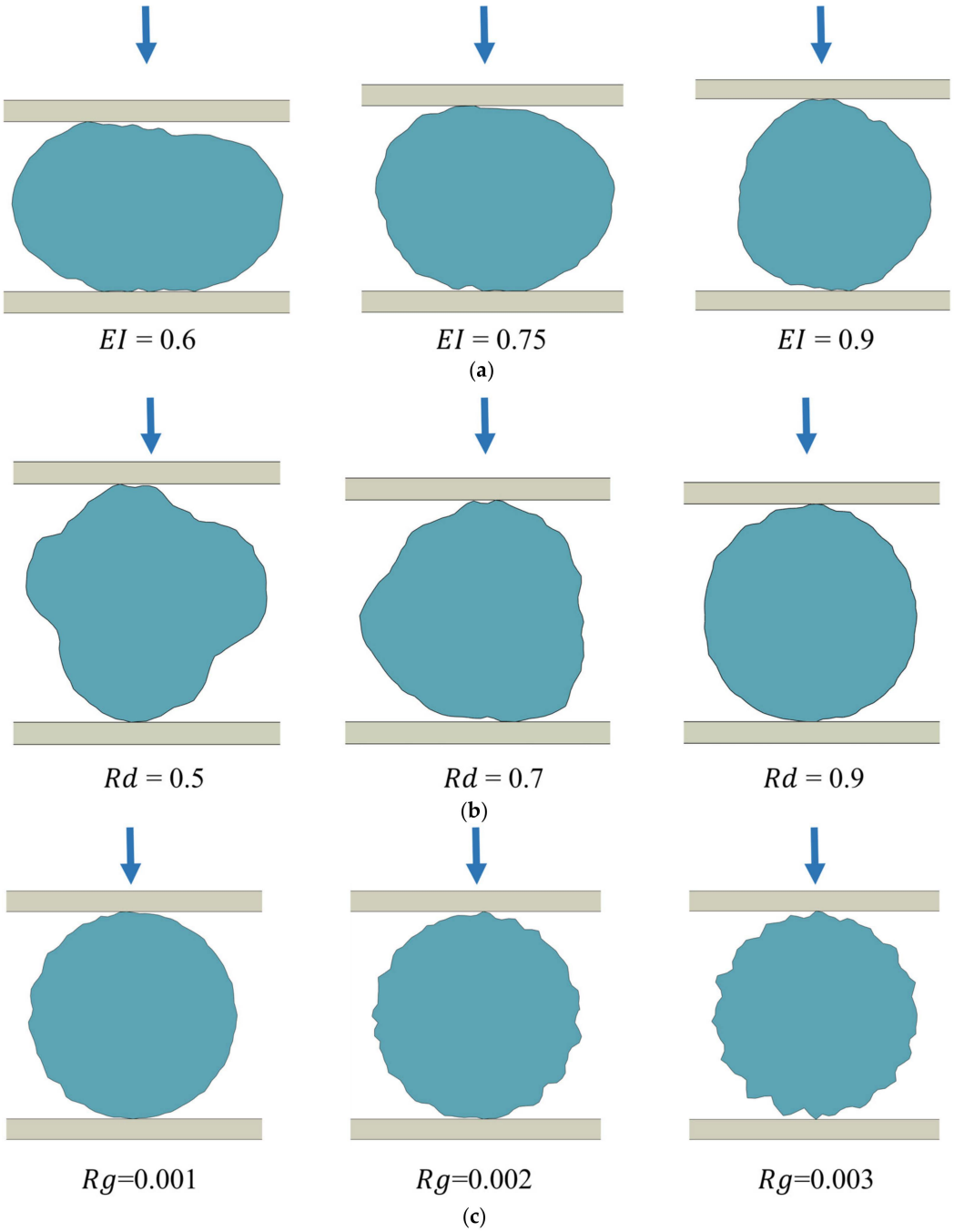

Figure 8. Particle profile reconstructed with different shape descriptors: (**a**) *EI*, (**b**) *Rd*, and (**c**) *Rg*.

Table 2. Scenarios for rock particles considering irregular shapes.

Shape Descriptors	Value	Number of Cases	Total
EI	0.6, 0.75, 0.9	20, 20, 20	60
Rd	0.5, 0.7, 0.9	20, 20, 20	60
Rg	0.001, 0.002, 0.003	20, 20, 20	60

To minimize the influence of particle size on simulation results, all particles were generated with a constant cross-sectional area. Prior to loading, each particle was rotated to an initial state corresponding to its minimum potential energy via moment of inertia alignment, ensuring maximum stability against rotational movement during compression. The particles were then positioned between two rigid loading plates: a fixed lower plate

and an upper plate that moved downward at a constant displacement rate of 0.1 mm/s (Figure 4). All models were discretized using triangular finite elements with a uniform mesh size of 1 mm, and cohesive elements were inserted throughout the domain to simulate fracture behavior. The material properties applied in these simulations were consistent with those listed in Table 1.

4. Results

4.1. Effects of Elongation Index on Particle Breakage

Figure 9a illustrates the cumulative survival probability of particles with varying elongation indices EI. The cumulative distribution of the fracture strength σ_f exhibits a consistent trend across different EI values, spanning a range of 1.2 MPa to 3.3 MPa. For reference, the dashed line represents the crushing strength of a disc-shaped particle with equivalent cross-sectional area. Notably, the mean crushing strength of particles with different EI values closely aligns with this reference value, suggesting that the influence of EI is not statistically significant. Figure 9b presents the simulated data points alongside their corresponding fitting curves derived from Formula (28) for different EI values. The data are well described by the Weibull distribution; however, the variations in the Weibull modulus m are negligible. Specifically, the Weibull moduli for $EI = 0.6$, 0.75, and 0.9 are 4.40, 5.06, and 4.61, respectively, indicating no substantial dependence on EI.

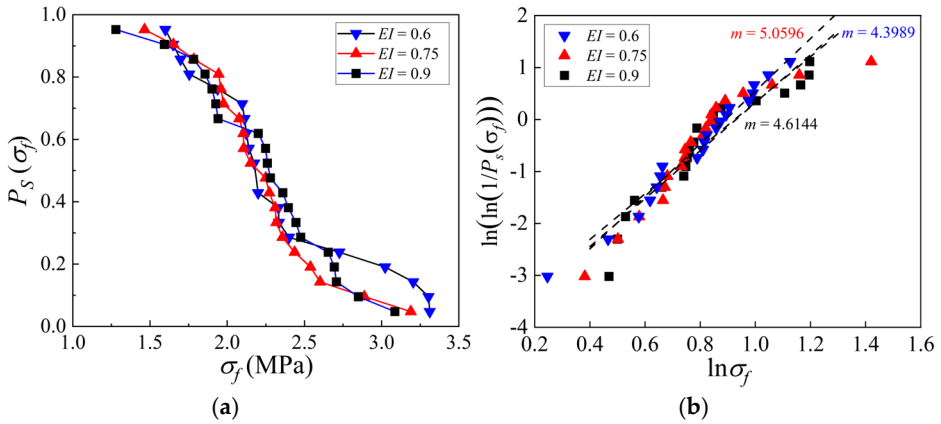

Figure 9. Single particle breakage with different EI (0.6, 0.75, and 0.9): (**a**) Particle survival probability and (**b**) Weibull distributions.

Further analysis of the relationship between mean fracture strength σ_f and EI (Figure 10a) confirms that the variation in particle crushing strength with EI is statistically insignificant, reinforcing the observations from Figure 9a. This suggests that macroscopic shape characteristics have a limited effect on σ_f, likely because particle breakage is predominantly governed by microscopic-scale features at the particle-loading plate interface. This hypothesis is further supported by the similar number of fragments N_f generated post-crushing across all EI groups (Figure 10b). In summary, the elongation index EI exhibits negligible influence on single-particle breakage behavior.

4.2. Effects of Roundness Index on Particle Breakage

Figure 11a presents the cumulative distributions of particle crushing strength σ_f for varying degrees of roundness Rd. The results demonstrate that σ_f increases with Rd, suggesting that irregular particle edges may induce stress concentration, thereby reducing crushing resistance. Furthermore, the mean crushing strengths for $Rd = 0.5$, 0.7, and 0.9 are 2.81 MPa, 3.36 MPa, and 3.69 MPa, respectively. These values consistently exceed those of disk-shaped particles, confirming that enhanced roundness improves particle crushing

strength. Figure 11b illustrates the Weibull distribution of σ_f across different Rd values. Notably, particles with higher Rd exhibit a lower Weibull modulus, implying that increased roundness correlates with greater variability in crushing strength.

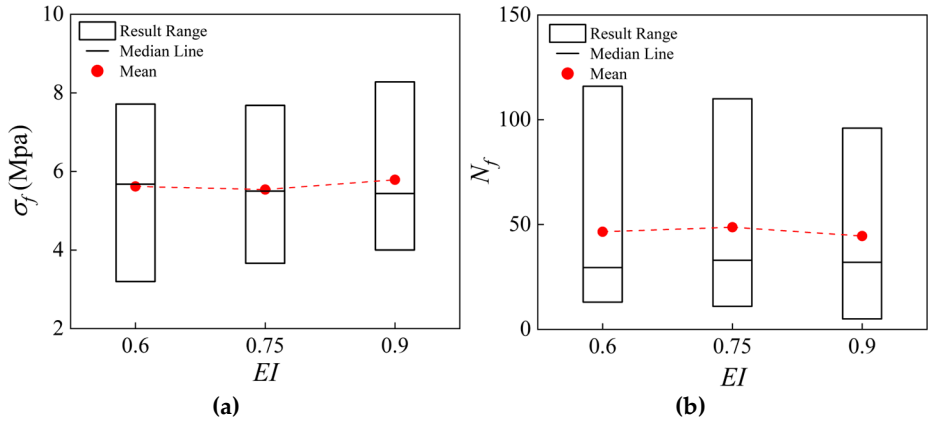

Figure 10. Single particle breakage with different EI (0.6, 0.75, and 0.9): (**a**) Variation of mean σ_f with EI and (**b**) Number of fragments N_f.

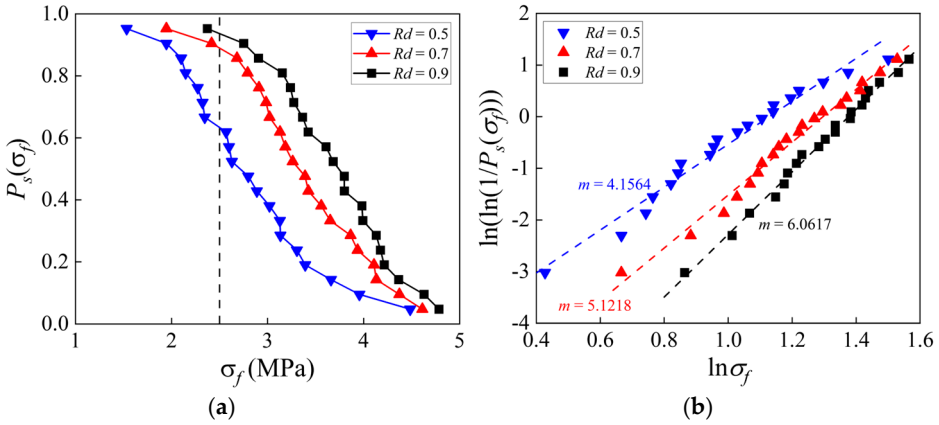

Figure 11. Single particle breakage with different Rd (0.6, 0.75, and 0.9): (**a**) Particle survival probability and (**b**) Weibull distributions.

Figure 12a depicts the relationship between fragment number N_f and Rd. As roundness increases, particles fracture into more numerous fragments, with a pronounced acceleration in fragmentation rate beyond $Rd = 0.7$. This behavior is attributed to the elastic strain energy E_E, stored within the particle prior to breakage. As shown in Figure 12b, higher roundness corresponds to greater E_E and reduced stress localization, promoting more extensive fragmentation along interfacial cohesive elements. Additionally, the variability in E_E increases with Rd, mirroring the trend observed for σ_f in Figure 11a, which suggests that E_E likewise follows a Weibull distribution. In conclusion, increasing Rd within the range of 0.5 to 0.9 enhances a particle's ability to withstand external loads, primarily due to improved energy absorption and more uniform stress distribution.

4.3. Effects of Roughness Index on Particle Breakage

Figure 13a presents the cumulative probability distributions of particle crushing strength σ_f for specimens with varying surface roughness Rg. The mean crushing strengths for all roughness conditions were observed to be significantly lower than the reference smooth-surface value, demonstrating that surface roughness substantially degrades particle crushing resistance. This phenomenon can be attributed to stress concentration effects at surface asperities, which facilitate crack initiation and propagation under loading condi-

tions. These findings are consistent with previous work by [48], who reported an inverse relationship between morphological complexity and characteristic crushing strength. The crushing strength distributions were found to follow the Weibull distribution with excellent goodness-of-fit, as shown in Figure 13b. Quantitative analysis revealed Weibull moduli of 4.1992 ± 0.12, 5.9988 ± 0.15, and 7.4095 ± 0.18 for Rg = 0.001, 0.002, and 0.003, respectively. The increasing Weibull modulus with greater Rg indicates reduced strength variability, suggesting that rougher surfaces produce more uniform stress concentration patterns. Microstructural analysis suggests these results from the proliferation of micro-asperities at higher Rg values, while smoother specimens (lower Rg) exhibit mixed stress concentration sites comprising both sharp corners and curved surfaces.

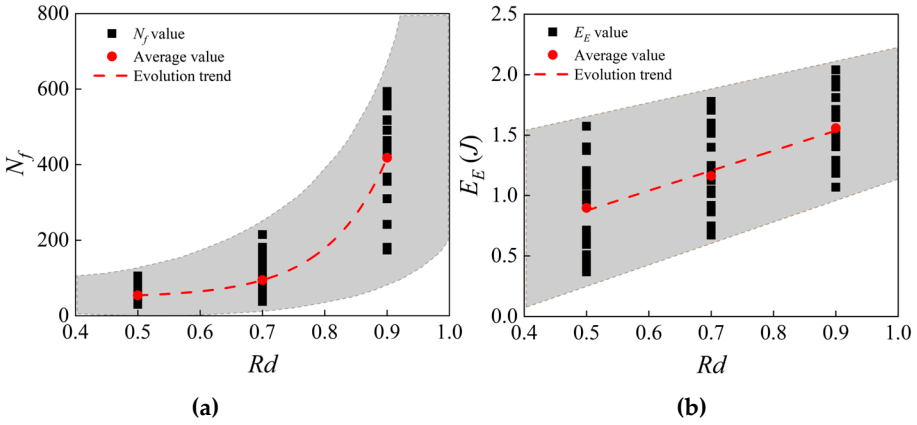

Figure 12. Single particle breakage with different Rd (0.6, 0.75, and 0.9): (**a**) Number of fragments N_f, and (**b**) Variation of elastic strain energy E_E.

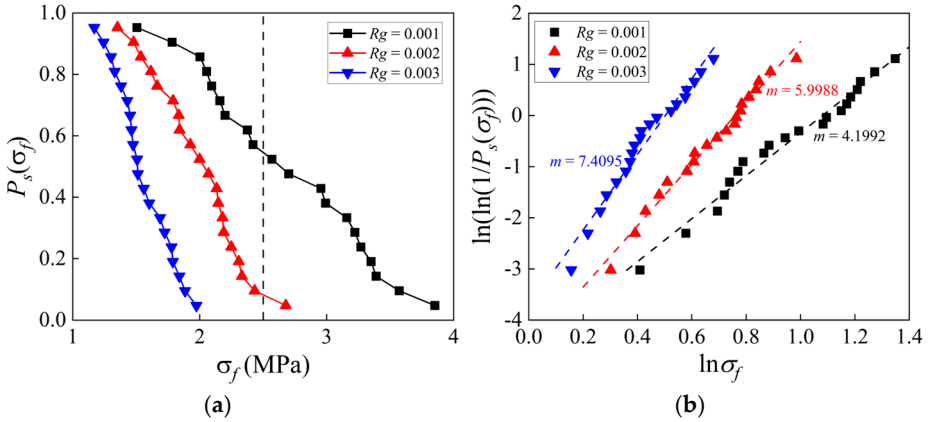

Figure 13. Single particle breakage with different Rg (0.6, 0.75, and 0.9): (**a**) Particle survival probability and (**b**)Weibull distributions.

Fragmentation analysis (Figure 14a) demonstrated a significant negative correlation between surface roughness and fragment count, with mean fragment numbers decreasing from 37 ± 2.1 to 20 ± 1.8 as Rg increased from 0.001 to 0.003. This trend was strongly correlated with the measured elastic strain energy E_E shown in Figure 14b, where E_E decreased from 0.92 ± 0.05 J to 0.30 ± 0.03 J over the same Rg range. These observations support the proposed fracture mechanism whereby surface roughness concentrates applied stresses at discrete asperities, leading to localized fracture initiation with reduced energy dissipation.

These results collectively demonstrate that increased surface roughness significantly compromises particle strength properties through two primary mechanisms: (1) introduction of stress concentration sites that reduce the critical load for fracture initiation, and (2) modification of fracture propagation patterns that limit energy absorption capacity.

The quantitative relationships established here provide important insights for materials design in applications where particle strength is a critical performance parameter.

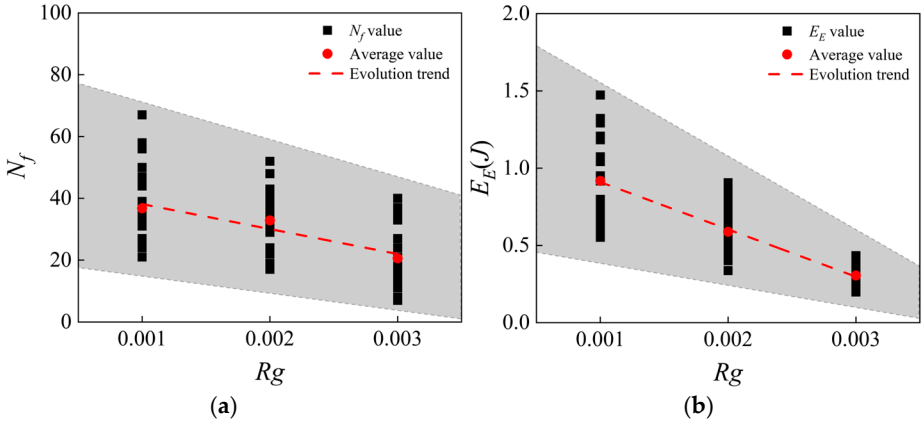

Figure 14. Single particle breakage with different Rg (0.6, 0.75, and 0.9): (**a**) Number of fragments N_f, and (**b**) Variation of elastic strain energy E_E.

4.4. Relationship Between Particle Crushing Strength and Fractal Dimension

Figure 15 illustrates the relationship between fractal dimension and particle crushing strength. As shown in the figure, the particle crushing strength decreases with increasing fractal dimension. This observation is consistent with the findings reported by Meng et al. [36], who noted that higher fractal dimensions indicate more pronounced particle defects, consequently leading to lower crushing strength. Generally, the fractal dimension exhibits an exponential negative correlation with crushing strength. However, in this study, a linear relationship was observed, which can be primarily attributed to the relatively narrow range of fractal dimensions examined. Within this limited span, the classical exponential decay approximates a linear relationship due to first-order Taylor expansion dominance, a phenomenon validated in granular materials with constrained morphological variance. This scale-dependent behavior contrasts with broader fractal dimension ranges, where full exponential decay manifests.

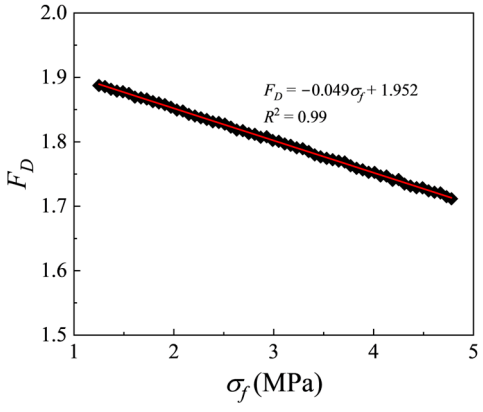

Figure 15. Variation of fractal dimension with particle crushing strength ($R^2 = 0.99$, $F_D = -0.049\sigma_f + 1.952$).

5. Conclusions

This study establishes an integrated computational framework combining Fourier-based shape reconstruction, fractal dimension analysis, and combined finite-discrete element method (FDEM) simulation. Using Fourier descriptor theory, particle morphology is efficiently parameterized based on harmonic coefficients, which directly correspond to

standardized shape descriptors—namely, the elongation index (EI), roundness index (Rd), and roughness index (Rg). Statistical consistency between synthesized particles and target morphological distributions is enforced via an inverse Monte Carlo sampling algorithm. This framework enables a systematic and quantitative investigation into the influence of particle morphology and fractal dimension on crushing strength and associated mechanical responses.

Variations in the EI within the range of 0.6 to 0.9 exert negligible influence on single-particle breakage characteristics. The mean crushing strength values for specimens with $I = 0.6$, $EI = 0.75$, and $EI = 0.9$ closely align with the reference value established for disc-shaped particles of equivalent area. Furthermore, the variation in fragment count remains statistically indistinct. Conversely, an increase in the Rd from 0.5 to 0.9 enhances particle resistance to external loading. This is evidenced by a concomitant increase in the Weibull modulus with Rd, signifying reduced variability in crushing strength for particles exhibiting higher Rd values. Notably, the mean crushing strength across all Rd groups exceeds the reference value. Additionally, both fragment count and stored elastic strain energy exhibit positive correlations with increasing Rd. In contrast, elevating the Rg within the range of 0.001 to 0.003 leads to diminished particle strength. The mean crushing strength for particles across Rg groups falls below the reference benchmark. Moreover, particle crushing strength demonstrates greater variability at elevated Rg levels. Concurrently, fragment count and stored elastic strain energy decrease as Rg increases. Notably, a negative correlation is observed between fractal dimension and particle crushing strength, suggesting that particles possessing a more complex fracture surface morphology tend to exhibit lower mechanical strength.

Author Contributions: Conceptualization, R.L. and S.H.; methodology, S.H.; software, R.L.; formal analysis, H.J.; data curation, N.Y.; writing—original draft preparation, R.L. and S.H.; writing—review and editing, S.H. and C.X.; supervision, S.H.; project administration, S.H. All authors have read and agreed to the published version of the manuscript.

Funding: This research received no funding.

Data Availability Statement: Data will be available upon reasonable request.

Conflicts of Interest: The authors declare no conflicts of interest.

References

1. Zhao, S.; Zhang, G.; Zhang, D.; Tan, D.; Huang, H. A hybrid attention deep learning network for refined segmentation of cracks from shield tunnel lining images. *J. Rock Mech. Geotech. Eng.* **2023**, *15*, 3105–3117. Available online: https://www.sciencedirect.com/science/article/pii/S1674775523001117 (accessed on 21 January 2024). [CrossRef]
2. Lin, W.; Sheil, B.; Zhang, P.; Zhou, B.; Wang, C.; Xie, X. Seg2Tunnel: A hierarchical point cloud dataset and benchmarks for segmentation of segmental tunnel linings. *Tunn. Undergr. Space Technol.* **2024**, *147*, 105735. [CrossRef]
3. Zeng, K.; Liu, H. Experimental Study on the Time-Dependent Oedometric Compression Behavior of Calcareous Sand. *J. Geotech. Geoenvironmental Eng.* **2023**, *149*, 04023025. [CrossRef]
4. Zeng, K.; Liu, H. Effect of Inherent Anisotropy on the Triaxial Compression Behavior of Coral Sand. *Int. J. Geomech.* **2023**, *23*, 04023033. [CrossRef]
5. Zeng, K.; Liu, H. Effect of particle size distributions on the mechanical behavior and particle breakage of coral sands. *Granul. Matter* **2023**, *25*, 44. [CrossRef]
6. Zeng, K.; Liu, H. Time-Dependent Characteristics of Coral Sand under Triaxial Stress States. *J. Geotech. Geoenvironmental Eng.* **2025**, *151*, 04024168. [CrossRef]
7. He, S.-H.; Yin, Z.-Y.; Ibraim, E.; Ding, Z. Face mask chips-reinforced sands under monotonic and cyclic torsional shearing. *Géotechnique* **2025**, 1–46. [CrossRef]
8. Liu, H.; Zeng, K.; Zou, Y. Particle Breakage of Calcareous Sand and Its Correlation with Input Energy. *Int. J. Geomech.* **2020**, *20*, 04019151. [CrossRef]

9. Zeng, K.; Yin, Z.-Y.; Li, R.; Jin, Y.-F. Role of particle morphology in monotonic and cyclic behavior of granular materials: Insights from cereals. *Powder Technol.* **2025**, *466*, 121452. [CrossRef]
10. He, S.-H.; Yin, Z.-Y.; Ding, Z.; Li, R.-D. Particle morphology and principal stress direction dependent strength anisotropy through torsional shear testing. *Can. Geotech. J.* **2024**, *62*, 1–23. [CrossRef]
11. He, S.-H.; Yin, Z.-Y.; Ding, Z.; Li, R.-D. Novel observations for the impact of particle morphology on shear modulus of granular materials. *Acta Geotech.* **2025**, *20*, 4631–4650. [CrossRef]
12. Zhou, X.-W.; Jin, Y.-F.; He, K.-Y.; Yin, Z.-Y. An improved explicit MPM formulation and its coupling scheme with FEM. *Comput. Methods Appl. Mech. Eng.* **2025**, *436*, 117734. [CrossRef]
13. Zhou, X.-W.; Jin, Y.-F.; He, K.-Y.; Yin, Z.-Y.; Liu, F.-T. A novel implicit FEM-MPM coupling framework using convex cone programming for elastoplastic problems. *Comput. Methods Appl. Mech. Eng.* **2024**, *429*, 117153. [CrossRef]
14. He, K.-Y.; Jin, Y.-F.; Zhou, X.-W.; Yin, Z.-Y. A high-performance semi-implicit two-phase two-layer MPM framework for modeling granular mass-water interaction problems. *Comput. Methods Appl. Mech. Eng.* **2024**, *427*, 117064. [CrossRef]
15. He, K.-Y.; Liang, W.; Yin, Z.-Y.; Jin, Y.-F. An efficient material point method framework based on the affine matrix. *Comput. Geotech.* **2023**, *163*, 105712. [CrossRef]
16. Liang, W.; He, K.-Y.; Jin, Y.-F.; Yin, Z.-Y. A gradient-smoothed material point method for reducing cell crossing noise in large deformation problems. *Comput. Geotech.* **2024**, *169*, 106169. [CrossRef]
17. He, K.-Y.; Jin, Y.-F.; Zhou, X.-W.; Yin, Z.-Y.; Chen, X. A generalized projection algorithm for overcoming volumetric locking in explicit material point method. *Comput. Geotech.* **2025**, *186*, 107391. [CrossRef]
18. Zhou, X.-W.; Jin, Y.-F.; Yin, Z.-Y.; Liu, F.-T.; Chen, X. A novel improved edge-based smoothed particle finite element method for elastoplastic contact analysis using second order cone programming. *Comput. Methods Appl. Mech. Eng.* **2025**, *441*, 118016. [CrossRef]
19. Liu, X.; Zeng, K.; Xiang, F.; Wang, C.; Hou, X.; Li, Y. Study on the interaction between particle shape and particle breakage of coral sand by discrete element method. *Front. Earth Sci.* **2024**, *12*, 1343307. [CrossRef]
20. Jiang, H.; Debanath, O.C.; Li, Y.; Li, R. A level-set method-based framework for modeling abrasion of railway ballast. *Transp. Geotech.* **2025**, *54*, 101628. [CrossRef]
21. Xu, C.; Wang, P.; Yin, Z.-Y.; Wen, Y.; Xu, C. Effect of particle shape on the mechanical behavior of methane hydrate-bearing sediments: A DEM study. *Comput. Geotech.* **2025**, *182*, 107141. [CrossRef]
22. Wang, P.; Xu, C.; Yin, Z.-Y.; Song, S.; Xu, C.; Dai, S. A DEM-based generic modeling framework for hydrate-bearing sediments. *Comput. Geotech.* **2024**, *171*, 106287. [CrossRef]
23. Kuang, D.-M.; Long, Z.-L.; Ogwu, I.; Chen, Z. A discrete element method (DEM)-based approach to simulating particle breakage. *Acta Geotech.* **2022**, *17*, 2751–2764. [CrossRef]
24. Brzeziński, K.; Gladky, A. Clump breakage algorithm for DEM simulation of crushable aggregates. *Tribol. Int.* **2022**, *173*, 107661. [CrossRef]
25. Harmon, J.M.; Arthur, D.; Andrade, J.E. Level set splitting in DEM for modeling breakage mechanics. *Comput. Methods Appl. Mech. Eng.* **2020**, *365*, 112961. [CrossRef]
26. Tang, Z.-Q.; Jin, Y.-F.; Yang, J.; Yin, Z.-Y.; Chen, X. Multi-physics two-layer SNS-PFEM for granular mass–water large deformation problems. *Int. J. Mech. Sci.* **2025**, *301*, 110492. [CrossRef]
27. Tang, Z.-Q.; Zhou, X.-W.; Jin, Y.-F.; Yin, Z.-Y.; Zhang, Q. A novel coupled bES-FEM formulation with SUPG stabilization for thermo-hydro-mechanical analysis in saturated porous media. *Comput. Geotech.* **2024**, *173*, 106454. [CrossRef]
28. Xi-Wen, Z.; Yin-Fu, J.I.N.; Kai-Yuan, H.E.; Zhen-Yu, Y.I.N. A convex cone programming based implicit material point method. *Comput. Methods Appl. Mech. Eng.* **2024**, *427*, 117007. [CrossRef]
29. Jiang, H.; Kawamoto, R.; Matsushima, T. Coupled effects of particle shape and inter-particle friction on quasi-static shear behavior of dry granular materials studied by 2D LS-DEM. *J. Struct. Eng. A* **2024**, *70*, 141–154.
30. Brown, G.J.; Miles, N.J.; Jones, T.F. A fractal description of the progeny of single impact single particle breakage. *Miner. Eng.* **1996**, *9*, 715–726. [CrossRef]
31. Arasan, S.; Akbulut, S.; Hasiloglu, A.S. The relationship between the fractal dimension and shape properties of particles. *KSCE J. Civ. Eng.* **2011**, *15*, 1219–1225. [CrossRef]
32. Tang, Z.-Q.; Yin, Z.-Y.; Jin, Y.-F.; Zhou, X.-W. A novel mesoscale modelling method for steel fibre-reinforced concrete with the combined finite-discrete element method. *Cem. Concr. Compos.* **2024**, *149*, 105479. [CrossRef]
33. Wadell, H. Volume, Shape, and Roundness of Rock Particles. *J. Geol.* **1932**, *40*, 443–451. [CrossRef]
34. Gadelmawla, E.S.; Koura, M.M.; Maksoud, T.M.A.; Elewa, I.M.; Soliman, H.H. Roughness parameters. *J. Mater. Process. Technol.* **2002**, *123*, 133–145. [CrossRef]
35. Zhang, W.; Sun, C.; Breckon, T.; Alshammari, N. Discrete Curvature Representations for Noise Robust Image Corner Detection. *IEEE Trans. Image Process.* **2019**, *28*, 4444–4459. [CrossRef]
36. Crownover, R.M. *Introduction to Fractals and Chaos*; Jones and Bartlett: Boston, MA, USA, 1995; ISBN 978-0-86720-464-3.

37. Li, J.; Du, Q.; Sun, C. An improved box-counting method for image fractal dimension estimation. *Pattern Recognit.* **2009**, *42*, 2460–2469. [CrossRef]
38. Mollon, G.; Zhao, J. 3D generation of realistic granular samples based on random fields theory and Fourier shape descriptors. *Comput. Methods Appl. Mech. Eng.* **2014**, *279*, 46–65. [CrossRef]
39. Su, D.; Yan, W.M. Quantification of angularity of general-shape particles by using Fourier series and a gradient-based approach. *Constr. Build. Mater.* **2018**, *161*, 547–554. [CrossRef]
40. Wang, X.; Liang, Z.; Nie, Z.; Gong, J. Stochastic numerical model of stone-based materials with realistic stone-inclusion features. *Constr. Build. Mater.* **2019**, *197*, 830–848. [CrossRef]
41. Li, R.; Yin, Z.-Y.; He, S.-H. 3D reconstruction of arbitrary granular media utilizing vision foundation model. *Appl. Soft Comput.* **2025**, *169*, 112599. [CrossRef]
42. Li, R.; Yin, Z.-Y.; He, S.-H.; Sheil, B. Enhancement and Assessment of Large Vision Models for 3D Particle Reconstruction from X-ray Tomography. *Can. Geotech. J.* **2025**, *62*, 1–28. Available online: https://cdnsciencepub.com/doi/abs/10.1139/cgj-2024-0736 (accessed on 8 April 2025). [CrossRef]
43. Metropolis, N.; Ulam, S. The Monte Carlo Method. *J. Am. Stat. Assoc.* **1949**, *44*, 335–341. [CrossRef]
44. Hiramatsu, Y.; Oka, Y. Determination of the tensile strength of rock by a compression test of an irregular test piece. *Int. J. Rock Mech. Min. Sci. Geomech. Abstr.* **1966**, *3*, 89–90. [CrossRef]
45. Weibull, W. A Statistical Distribution Function of Wide Applicability. *J. Appl. Mech.* **1951**, *18*, 293–297. [CrossRef]
46. Weibull, W. *A Statistical Theory of the Strength of Materials*; Generalstabens Litografiska Anstalts Förlag: Stockholm, Sweden, 1939; Available online: https://books.google.com.hk/books?id=otVRAQAAIAAJ (accessed on 8 April 2025).
47. *Abaqus User Manual*; Abacus: Sydney, Australia, 2020.
48. Wu, X.; Wang, G.; Li, G.; Han, W.; Sun, S.; Zhang, S.; Bi, W. Research on Shear Behavior and Crack Evolution of Symmetrical Discontinuous Rock Joints Based on FEM-CZM. *Symmetry* **2020**, *12*, 1314. [CrossRef]